



RESEARCH ARTICLE | JULY 20 2022

An investigation of a gas–liquid swirling flow with shear-thinning power-law liquids

Shuo Liu (刘硕) ; Jian Zhang (张健)  ; Jing-yu Xu (许晶禹) 



Physics of Fluids 34, 073320 (2022)

<https://doi.org/10.1063/5.0099895>



View
Online



Export
Citation

CrossMark

Articles You May Be Interested In

Binaural sensitivity as a function of interaural electrode position with a bilateral cochlear implant user

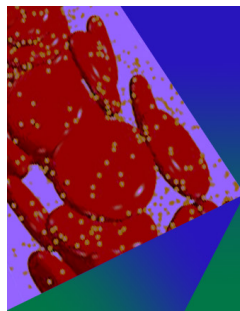
J Acoust Soc Am (August 2003)

Computer simulation of diffraction focusing in proximity lithography

AIP Conference Proceedings (December 2019)

Squeeze flow of a Carreau fluid during sphere impact

Physics of Fluids (July 2012)



Physics of Fluids

Special Topic: Flow and Forensics

Submit Today!

An investigation of a gas–liquid swirling flow with shear-thinning power-law liquids

Cite as: Phys. Fluids **34**, 073320 (2022); doi: 10.1063/5.0099895

Submitted: 19 May 2022 · Accepted: 1 July 2022 ·

Published Online: 20 July 2022



View Online



Export Citation



CrossMark

Shuo Liu (刘硕),¹  Jian Zhang (张健),^{1,a)}  and Jing-yu Xu (许晶禹)^{1,2,a)} 

AFFILIATIONS

¹Institute of Mechanics, Chinese Academy of Sciences, Beijing 100190, China

²School of Engineering Sciences, University of Chinese Academy of Sciences, Beijing 100049, China

^{a)}Authors to whom correspondence should be addressed: zhangjian@imech.ac.cn and xujingyu@imech.ac.cn

ABSTRACT

A gas–liquid swirling flow with shear-thinning liquid rheology exhibits complex behavior. In order to investigate its flow characteristics, experiments and computational fluid dynamics (CFD) simulations are conducted based on dimensional analysis. A Malvern particle size analyzer and electrical resistance tomography are applied to obtain the bubble size distribution and section void fraction. A Coriolis mass flowmeter is applied to obtain the mixture flow rate and mixture density for an entrance gas volume fraction smaller than 7%. The CFD coupled mixture multiphase model and large eddy simulation model are applied, considering the liquid shear-thinning power-law rheology. The results show that the swirling flow can be divided into developing and decaying sections according to the swirl intensity evolution in the axial direction. A gas–liquid swirl flow with shear-thinning liquid prohibits a core-annulus flow structure. A smaller index n contributes to maintaining the development of the swirl flow field and its core-annulus flow structure so that the swirl flow can form over a shorter distance with a stronger intensity. For a more uniform distribution of the apparent viscosity, the gas column in the pipe center is thinner. On the other hand, a larger consistency k enlarges the stress tensor. The amplitude of the velocity and the pressure of the core-annulus flow structure are reduced. A weaker swirl intensity appears with a wider gas column appearing as a consequence. Furthermore, the swirl number decays with an exponential behavior with parameters sensitive to the consistency k and index n of the decaying section of the swirling flow field. These are beneficial to gas–liquid separator design and optimization when encountering the shear-thinning power-law liquid phase in the petroleum industry.

Published under an exclusive license by AIP Publishing. <https://doi.org/10.1063/5.0099895>

I. INTRODUCTION

A gas–liquid swirling flow in a pipe will exhibit complex flow behavior.¹ Its unique flow properties, brought about by tangential momentum, have a wide range of applications in nuclear energy, petroleum exploration, and power technology such as phase separation, turbulent mixing, heat transfer, and the conveying of particles.^{2–5} An axially induced swirling flow field, in particular, has pressure drop, space demand, and structure simplicity advantages over other swirling-inducing methods, and has, therefore, attracted a great deal of focus from researchers.⁶ To reveal the gas–liquid swirling flow mechanism and to take advantage of its flow characteristics, a series of works have been proposed on flow pattern transitions, momentum transfer, swirl strength decay, and structure design.^{7–11} Scientific questions are usually proposed on the basis of industrial applications. In on-site applications, the liquid phase viscosity may not always be kept constant. For instance, certain kinds of crude or processed liquids with chemical agents may show non-Newtonian rheology properties, such

as shear-thinning properties. When a gas–liquid swirling flow is encountered in such cases, an investigation of its flow characteristics is important to the aim of understanding its mechanism and potential applications.¹²

Similar to a surface vortex, a swirling flow in a pipe consists of a core region and an annulus region. In the core region, a forced vortex is predominant, while in the annulus region, a free vortex is predominant.^{1,13} In 1964, an analytical solution for a vortex in a laminar flow that considered viscosity was proposed.¹³ Uberoi *et al.* conducted subsequent modifications to this.¹⁴ Beauber *et al.* proposed an analytical–numerical solution for a freely decaying laminar swirling flow.¹⁵ When the Reynolds number keeps increasing so that the flow turns into a turbulent flow, Reynolds stress terms are included, making the Navier–Stokes (N–S) equation more complicated. When restricted to a pipe, a combination of streamline curvature and flow skewness has significant effects on turbulence, making additional theoretical and experimental studies of urgent importance.¹ Under such conditions,

hot-wire probes, particle image velocimetry (PIV), and laser Doppler velocimetry (LDV) have been applied to acquire velocity distributions and the Reynolds stress.^{1,16,17} With the development of computer science, computational fluid dynamics (CFD) has become a practical method with which to characterize turbulent swirling flow in pipes. By comparing several two-equation turbulence models and the Reynolds stress model (RSM) for simulating a swirling flow field in a pipe, Cai *et al.* found that the RSM model performs better than the other two-equation turbulence models.⁶ In terms of near-wall treatment, wall functions with profiles that follow a log law have been found to agree well for moderately swirling pipes.¹⁸ Furthermore, the large eddy simulation approach has been applied in pipe swirling flow simulations as it performs better in capturing the transient phenomena or detailed structures of the turbulent flow.^{10,19,20} In a gas–liquid swirling flow, beyond the velocity distribution, the void fraction is another important flow parameter. To obtain the void fraction distribution in a swirling flow pipe, digital image processing, electrical resistance tomography (ERT), and wire-mesh sensors have all been applied.^{4,5,7} Liu *et al.* proposed a theoretical model for characterizing the decay of a gas–liquid swirling flow.⁷

Such a flow may show non-Newtonian rheology properties in cases of crude or processed fluids with additive agents. Under such conditions, the former linear stress–strain relationships vary according to the liquid phase rheology properties. Take shear-thinning power-law fluids for instance, which are always encountered in drilling hydraulics.²¹ When the index n is smaller than 1, the rheology turns into that of a shear-thinning fluid. The rate of decay of the turbulence will change proportionally to the n th power of the liquid rate of shear.²² In order to investigate the power-law fluid flow behavior in a pipe, quantitative researchers have contributed their efforts. For instance, Chebbi developed an analytical model predicting the pressure drop and velocity distribution of a laminar flow in a circular pipe with power-law rheology.²³ Yanuar *et al.* applied a pressure sensor to obtain the pressure drop of a power-law mudflow in a spiral pipe and found that a spiral pipe was more effective than a circular pipe with a combination of a rheology model and test data.²⁴ Most recently, Sorgun *et al.* proposed mechanical models to predict the pressure drop of power-law fluids and Herschel–Bulkley fluids flowing in a rough pipe.²⁵ For swirling flows, Dyakowski *et al.* conducted a laminar simulation of a non-Newtonian flow in a hydrocyclone and discussed the influence of fluid rheology on the fluid domain.²⁶ Yang *et al.* discussed the influence of liquid power-law properties on the turbulent hydrocyclone fluid domain.²⁸ Filip and David provided a quasisimilarity solution for a helical power-law fluid flow in concentric annuli with a rotating inner cylinder.²⁷ Taheran and Javaherdeh conducted an experiment to investigate the influence of a swirling generator on the heat transfer and pressure drop of a non-Newtonian nanofluid.²⁹

Beyond the above work on the fluid domain of a swirling flow with non-Newtonian fluids, publications on gas–liquid axial-induced swirling flows with shear-thinning power-law fluids are rare. In fact, the phase distribution, together with velocity distribution and the swirl intensity decay, are of crucial importance to the fluid domain. An investigation of fluid physics to reveal the characteristics of gas shear-thinning power-law liquid swirling turbulent flows is still urgently needed. This work, therefore, presents a systematic experimental test and CFD analysis to detect the characteristics of such a flow and the mechanisms behind them.

II. EXPERIMENTAL METHODS

A. Vortex inducing equipment and dimensionless analysis

An axial gas–liquid swirling flow field in a pipe is induced by a vane zone, which includes a hub and several blades embedded in a pipe. As shown in Fig. 1, the characteristic geometry parameters are as follows:

- pipe diameter, $D[L] = 100$ mm;
- pipe length, $L[L] = 1.9$ m;
- blade angle exit edge and pipe center, $\beta_1 = 45^\circ$;
- blade length, $L_h[L] = 1100$ mm; and
- hub diameter, $D_h[L] = 50$ mm.

The rheology model of a power-law fluid is given by

$$\tau = k\dot{\gamma}^n, \tag{1}$$

in which τ is the shear stress, k is the consistency, n is the index, and $\dot{\gamma}$ is the rate of shear of the liquid. When n is smaller than 1, the equation above is a model for shear-thinning power-law fluids. The apparent viscosity μ_{app} can then be expressed as

$$\mu_{app} = k\dot{\gamma}^{n-1}. \tag{2}$$

The flow variables are as follows:

- mixture entrance velocity, $U_0[L T^{-1}]$;
- mixture tangential velocity, $u_t[L T^{-1}]$;
- mixture axial velocity, $u_z[L T^{-1}]$;
- liquid density, $\rho_l [M L^{-3}]$;
- liquid shear rate, $\dot{\gamma}[T^{-1}]$;
- liquid consistency, $k[M L^{-1} \cdot T^{n-2}]$;
- gas density, $\rho_g[M L^{-3}]$;
- void fraction, $\alpha_g[-]$;
- gas apparent viscosity, $\mu_g[M L^{-1} T^{-1}]$;
- pressure, $P[M L T^{-2}]$; and
- cylinder coordinate system, $r[L], \theta[-], z[L]$.

Subsequently, in a relatively stable swirling flow field, the velocity components and pressure in the fluid domain can be characterized by

$$[u_z, u_t, p] = f(r, z, \theta, D, L, \beta_1, L_h, D_h, U_0, \rho_l, \mu_{app}, \rho_g, \alpha_g, \mu_g). \tag{3}$$

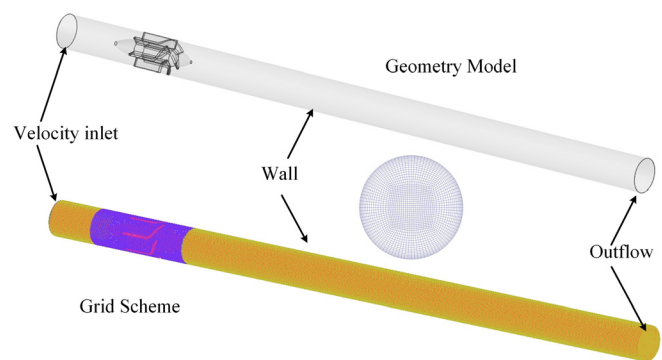


FIG. 1. Geometry model and grid scheme.

Downloaded from http://pubs.aip.org/aip/pof/article-pdf/doi/10.1063/5.0099895/1664318/073320_1_online.pdf

Assuming the vortex-inducing configuration to be fixed, and taking D , U_0 , and ρ_l as basic parameters gives

$$\left[\frac{u_z}{U_0}, \frac{u_t}{U_0}, \frac{p - p_0}{1/2 \rho_l U_0^2} \right] = f \left(\frac{r}{D}, \frac{z}{D}, \theta, \frac{\mu_{app}}{\rho_l U_0 D}, \frac{\rho_g}{\rho_l}, \alpha_g, \frac{\mu_g}{\mu_{app}} \right), \quad (4)$$

in which ρ_g/ρ_l is fixed when the fluids types are constrained, μ_g/μ_{app} becomes a variable dependent on the Reynolds number at the same time. Consequently, the dimensionless velocity components and pressure are determined by the coordinate location, the Reynolds number, and the gas void fraction, that is,

$$[u_z^*, u_t^*, p^*] = f(r^*, z^*, \theta, Re, \alpha_g). \quad (5)$$

The Re of a power-law fluid can be defined as

$$Re = \frac{\rho_m u_m^{2-n} D^n}{k}, \quad (6)$$

in which ρ_m is the mixture density and u_m is the mixture velocity. For further analysis, an experimental test and CFD are conducted using the parameters above.

B. Testing flow loop

A flow experiment was conducted on a self-circulation system. As shown in Fig. 2, a liquid tank and air compressor provided liquid and gas to the flow loop. The liquid in the liquid tank was motivated by a centrifugal pump, and the flow rate was measured by a turbine flow meter. Gas from the air compressor was measured using a thermal mass flowmeter and was then added to the main flow loop to be fully mixed with the liquid phase in the static mixer (SV-5/100) whose

inner diameter D_{in} and length H_s were 100 mm, hydraulic diameter D_h was 5 mm, and static mixture porosity α_{sp} was 1 approximately. Subsequently, the density of the fluid and the flow rate of the mixture were measured using a Coriolis mass flowmeter, and the mixture flowed into a horizontally mounted testing section. In the testing section, two pressure gauges were mounted at the entrance to measure the pressure drop. Inline sampling equipment was mounted upstream of the vane zone to measure the entrance bubble size distribution using the Malvern particle size analyzer. Downstream of the vane zone, an electrical resistance tomography (ERT) sampling electrode was mounted to test the section void fraction of the fluid domain. Subsequently, the liquid mixture exited the testing section and was injected into the liquid tank again. The pipe diameter of the flow loop was 50 mm, whereas the diameter of the testing section was 100 mm, with necking connecting them together.

C. Working fluids

In the experiment, air provided by the compressor acted as the gas phase. Water and sodium dodecyl sulfate (SDS) solution with various concentrations (1000 and 2000 mg/l) were used as the liquid phase. Under indoor environmental conditions, the density of the liquid phase was 998.1 kg/m^3 , while the density of the gas phase was 1.25 kg/m^3 . Figure 3 shows the rheology properties of working fluids with different SDS concentrations obtained from the Hake 6000 s rheometer. It is obvious that shear thinning power-law properties can be observed under such conditions. When C_{SDS} is 1000 mg/l, the consistency k is 0.01337 Pa s^n , and the index n is 0.80557 with an R -square of 0.99936. When C_{SDS} is 2000 mg/l, the consistency k is 0.02721 Pa s^n , and the index n is 0.66209 with an R -square of 0.99768. It can be

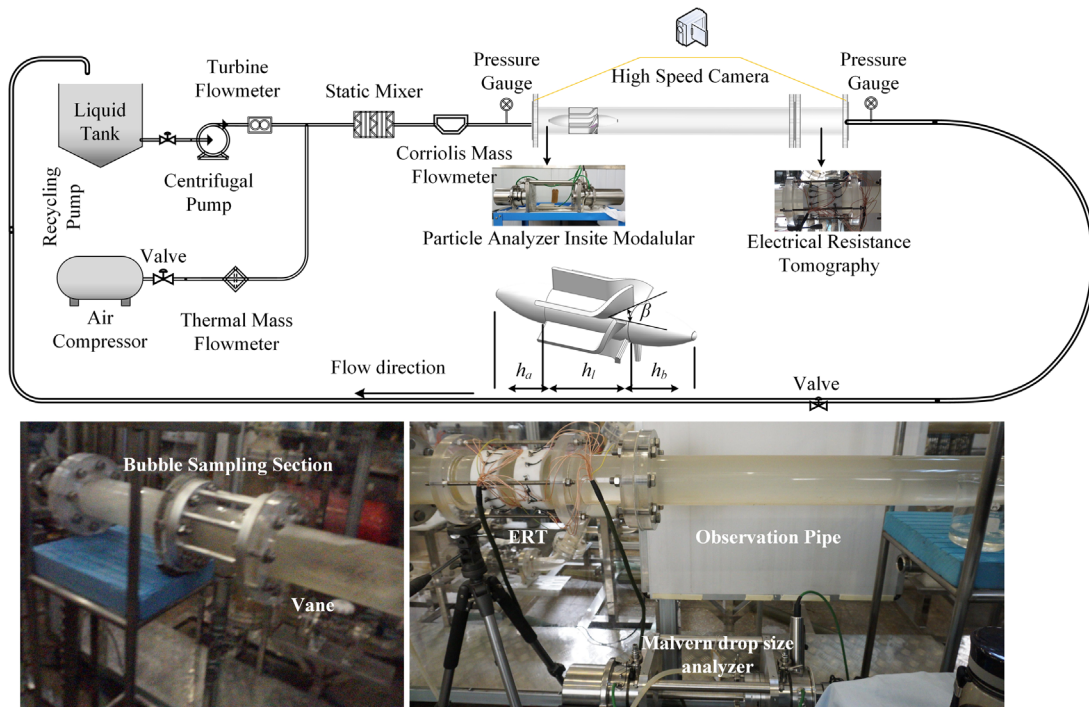


FIG. 2. Experiment flow loop, vane configuration, and key measuring equipment.

Downloaded from http://pubs.aip.org/aip/pof/article-pdf/doi/10.1063/5.0099895/16643118/073320_1_online.pdf

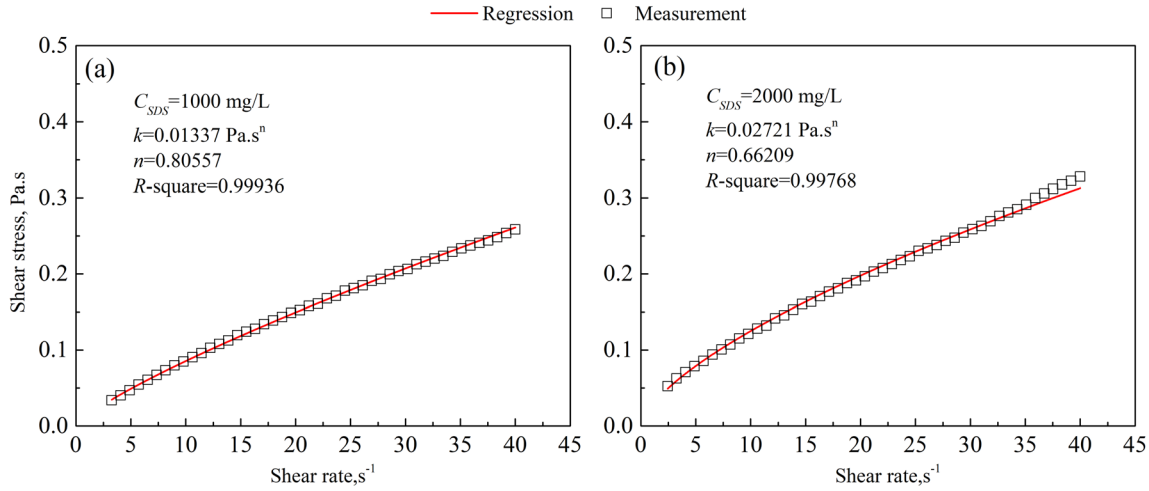


FIG. 3. Rheology properties with different SDS concentrations [(a) $C_{SDS} = 1000$ mg/l; (b) $C_{SDS} = 2000$ mg/l].

observed that an increment in C_{SDS} induces a rise in the consistency k while reducing the index n .

D. Measurement method and systematic errors

In the experiment, the mixture density and flow rate of a gas–liquid flow were measured using a Coriolis mass flow meter (Emerson MicroMotion F050). The error associated with the mass flow rate is 0.10% and that associated with the density is 0.5 kg/m³.

The bubble size distribution was measured using the Malvern particle size analyzer (Insitex). Using the Malvern particle size analyzer, the bubble size distribution curve could be obtained together with the bubble characteristic size d_{32} , also known as the Sauter diameter. An unideal mounted lens may raise the bubble size error to up to 15% according to Hirleman.³⁰

The void fraction was measured using ERT (EIT 3000). With the electrical conductivity variance of the cross-section being acquired by an electrode mounted around the pipe wall, the phase distribution can be obtained through a phase reconstruction matrix. The systematic error associated with ERT can be up to 10% according to work conducted by Wang *et al.*³¹

E. Operating condition settings

The liquids considered in the experiment were pure water, 1000 mg/l SDS solution, and 2000 mg/l SDS solution. Given certain SDS solution concentrations, the liquid entrance flow rate was adjusted from 16 to 18 m³/h, while the entrance gas volume fraction was controlled to within 10%. Correspondingly, the entrance mixture Reynolds number varied from 3900 to 65 000, following the Reynolds number model for a power-law fluid as shown in Eq. (6).

III. NUMERICAL METHODS

A. CFD model

Because a gas shear-thinning power-law liquid turbulent swirling flow is very intricate, CFD is essential to characterizing its fluid domain properties. To solve the gas–liquid N–S equations, a multi-phase model should first be specified. According to previous works,

the mixture multiphase model can characterize a gas column in a swirling flow field with acceptable accuracy.^{4,32,33} The equations of the mixture model are as follows:³⁴

$$\frac{\partial \rho_m}{\partial t} + \nabla \cdot (\rho_m \vec{v}_m) = 0, \tag{7}$$

$$\rho_m = \sum_{k=1}^n \alpha_k \rho_k, \tag{8}$$

$$\vec{v}_m = \frac{\sum_{k=1}^n \alpha_k \rho_k \vec{v}_k}{\rho_m}, \tag{9}$$

$$\mu_m = \sum_{k=1}^n \alpha_k \mu_k, \tag{10}$$

$$\frac{\partial (\rho_m \vec{v}_m)}{\partial t} + \nabla \cdot (\rho_m \vec{v}_m \vec{v}_m) = -\nabla p + \nabla \cdot \left[\mu_m (\nabla \vec{v}_m + \nabla \vec{v}_m^T) \right] + \rho_m \vec{g} + \nabla \cdot \left(\sum_{k=1}^n \alpha_k \rho_k \vec{v}_{dr,k} \vec{v}_{dr,k} \right). \tag{11}$$

In the above, ρ is the density, \vec{v} is the velocity vector, μ is the viscosity, the subscript m represents the mixture value, the apparent viscosity of the liquid μ_1 is calculated according to Eq. (2), k represents the k th phase, and $\vec{v}_{dr,k}$ is the drift velocity of the k th phase, obtained using the equation below:

$$\vec{v}_{dr,k} = \vec{v}_k - \vec{v}_m. \tag{12}$$

For the turbulence model, a large eddy simulation was applied because of its better performance in characterizing the transient properties of the fluid domain.^{10,19} For incompressible flows, filtering the time-dependent N–S equations, the governing equations are as follows:²¹

$$\frac{\partial (\rho \bar{u}_i)}{\partial x_i} = 0, \tag{13}$$

$$\frac{\partial (\rho \bar{u}_i)}{\partial t} + \frac{\partial (\rho \bar{u}_i \bar{u}_j)}{\partial x_j} = -\frac{\partial \bar{p}}{\partial x_i} + \rho g_i + k \frac{\partial}{\partial x_j} \left[\gamma^{n-1} \left(\frac{\partial \bar{u}_i}{\partial x_j} + \frac{\partial \bar{u}_j}{\partial x_i} \right) \right] - \frac{\partial \tau_{ij}}{\partial x_j}, \tag{14}$$

where τ_{ij} is the subgrid-scale stress and can be expressed as

$$\tau_{ij} = \frac{1}{3} \tau_{kk} \delta_{ij} - 2 \bar{S}_{ij} \rho L_s^2 \left[\frac{(S_{ij}^d S_{ij}^d)^{2/2}}{(\bar{S}_{ij} \bar{S}_{ij})^{5/2} + (S_{ij}^d S_{ij}^d)^{5/4}} \right]. \quad (15)$$

In wall-adapting local eddy-viscosity (WALE) models, it can be defined as

$$\bar{S}_{ij} = \frac{1}{2} \left(\frac{\partial \bar{u}_i}{\partial x_j} + \frac{\partial \bar{u}_j}{\partial x_i} \right), \quad (16)$$

$$L_s = \min(\kappa d, C_w V^{1/3}), \quad (17)$$

$$S_{ij}^d = \frac{1}{2} \left[\left(\frac{\partial \bar{u}_i}{\partial x_j} \right)^2 + \left(\frac{\partial \bar{u}_j}{\partial x_i} \right)^2 \right] - \frac{1}{3} \delta_{ij} \left(\frac{\partial \bar{u}_k}{\partial x_k} \right)^2, \quad (18)$$

where κ is the von Kármán constant, whose value is 0.41, d is the distance to the wall, C_w is the WALE constant, and V is the volume of the grid.

B. Geometry model and mesh scheme

Figure 1 shows the geometric model and grid scheme applied in this work. The geometric model consists of a cylindrical pipe, with locations corresponding to the blades and hub being hollowed. As the geometric structure of the vane zone is complicated, a mixture cell scheme that was successfully used to predict droplet size distribution parameters in our previous work was applied.³⁵ Grids corresponding to the fluid domain around the vane zone were created in an unstructured manner, while grids in the rest of the fluid domain were created in a structured manner using the O-grid method. Furthermore, grids near the wall were refined to better characterize the near-wall flow characteristics.

In order to check the accuracy of the grid scheme, a grid-independence test was conducted. As in our previous work, three schemes were applied to the simulation conditions with the entrance Reynolds number set to 64 377. The three different grid schemes are a coarse scheme (83.3 thousand grids), a medium scheme (1.74×10^6), and a fine scheme (2.26×10^6). These were applied to the radial pressure and tangential velocity $8D$ downstream of the vane zones to compare the CFD results for different grid schemes. As shown in Fig. 4, for both the pressure and tangential velocity, the profiles obtained with the medium and fine schemes were nearly identical, while a great discrepancy appeared between the coarse and medium schemes. This means that the medium grid scheme is sufficient for conducting the CFD investigation and this scheme was adopted.

C. Solution setting

Following the above discussion, the mixture multiphase model coupled with the LES turbulent model was applied to solve the gas–liquid N–S equations. The primary phase was liquid, and the secondary phase was gas. The bubble diameter was set from measuring data obtained with the Malvern particle size analyzer. Furthermore, the shear-thinning power-law rheology model of the liquid phase was encoded in the solving equations.

The CFD cases were conducted in a transient manner. In unsteady fluid domain simulations, the Courant number should be enforced to be smaller than one when determining the time step size.³⁶ Consequently, the time step size was set to 0.1 ms, considering the relatively low entrance velocity and keeping the Courant number smaller than 0.25. The simulations were performed over 8 s to ensure the stability of the fluid domain.

In terms of discrete schemes, the SIMPLE algorithm was applied to the pressure–velocity coupling and PRESTO was applied as a press

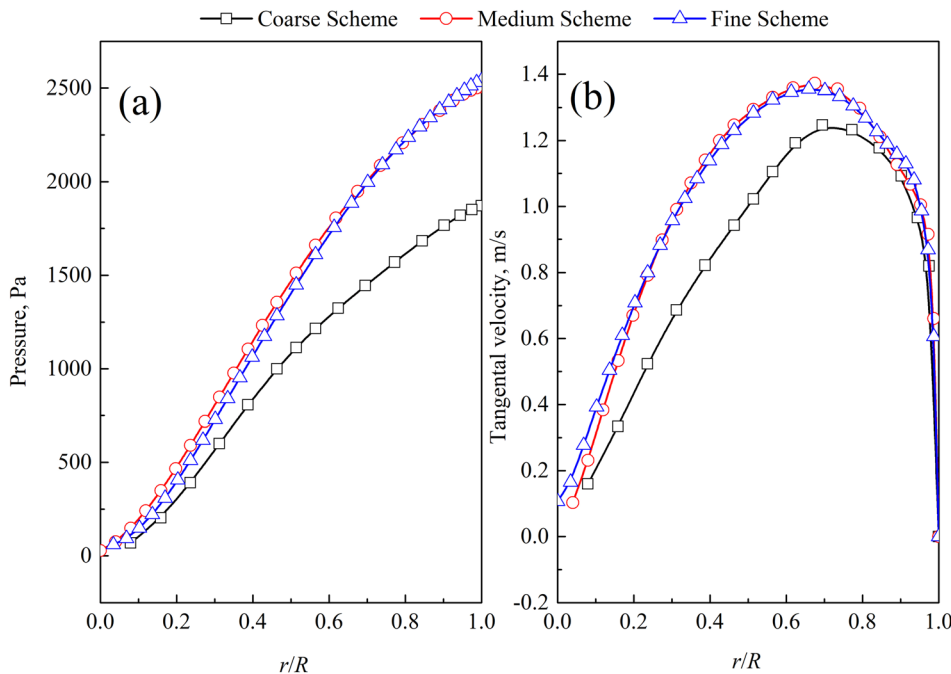


FIG. 4. Grid independent study $8D$ downstream vane zone [(a) pressure; (b) tangential velocity].

TABLE I. Operating parameters in CFD.

Case No.	Inlet flow rate (m ³ /h)	Inlet velocity (m/s)	Reynolds number	Gas concentration (%)	Power-law fluid parameter		bubble diameter (μm)
					<i>k</i> (Pa s ^{<i>n</i>})	<i>n</i>	
1	18.2	0.644	64 280	5.4	0.001 00	1.000 00	1047.67
2	18.4	0.651	6997	6.5	0.013 37	0.805 57	902.93
3	16.5	0.584	3888	6.7	0.027 21	0.662 09	1264.07
4	18.4	0.651	25 447	6.5	0.013 37	0.080 56	902.93
5	18.2	0.644	3732	5.4	0.020 00	0.890 00	1047.67
6	18.2	0.644	5836	5.4	0.020 00	0.650 00	1047.67

discretization scheme. The bounded central differencing was applied as the momentum scheme,¹⁹ and QUICK was applied as the volume fraction discretization scheme. Finally, the bounded second-order implicit scheme was applied as the transient formulation discretization scheme. In addition, the residuals of the equations were set to be 10⁻⁶ to ensure sufficient accuracy.

D. Boundary conditions and operating parameter settings

For the boundary conditions, the entrance of the fluid domain was set as the velocity inlet, with the velocity and volume fraction being set. The exit of the fluid domain was set as the outflow, considering that the vortex continues to exist after flowing out of the fluid domain. Other surfaces corresponding to the pipe wall and blades were set as stationary walls.

The operating parameters in the CFD were set in correspondence with test results. Relevant conditions were also simulated in order to investigate the influence of the power-law consistency *k* and index *n*. All of the operating parameters can be seen in Table I. In Table I, cases 1–3 were arranged on the basis of testing data. Cases 4–6 were derivate cases determined on the basis of cases 1 and 2 to show the influence of rheology parameters on the swirling flow properties.

IV. RESULTS AND DISCUSSION

A. *D*₃₂ variation at swirl flow entrance

Our previous work has proposed a bubble *d*₃₂ prediction model [Eq. (19)] suitable for bubble flow with Newtonian liquids.⁴ However, in power-law shear-thinning fluids, the model may be unsuitable. On the basis of bubble size distribution obtained by the Malvern droplet analyzer, a modified prediction model is proposed in the form of Eq. (20) to include the influence of power-law rheology. In the equation, *Re*_{*h*} is the power-law fluid Reynolds number of the static mixer obtained by Eq. (6), and *We*_{*h*} is the Weber number which can be obtained by Eq. (21),

$$\frac{d_{32}}{D_h} = 0.15 We_h^{-0.5} Re_h^{0.15}, \tag{19}$$

$$\frac{d_{32}}{D_h} = 0.25 We_h^{-0.5} Re_h^{0.15}, \tag{20}$$

$$We_h = \frac{\rho_m u_m^2 D_h}{\sigma \alpha_{sp}^2}, \tag{21}$$

in which σ is the surface tension coefficient. According to Fig. 5, the model in this work gets better prediction within the ±20% error range compared to our previous model. The discrepancy results from the liquid rheology property. Our previous work is suitable for Newtonian fluids, whereas the model in this work considers power-law rheology in the calculation of *Re*_{*h*}.

B. CFD validation

CFD validation was conducted from two perspectives. The first was the gas phase distribution. Figure 6 shows comparisons between the CFD and experimental observations. From observation of the testing section, it is obvious that a gas column appears in the center of the swirling flow field. In the void fraction contour, the gas column appears as it was in the photo observation. Due to light diffraction by the round pipe, the gas column in the photo may be slightly thinner than that in the CFD. As is illustrated in Fig. 6(d), the gas-liquid mixture entered the fluid domain, then flowed into the vane zone with the fluid twisting along the blades. After exiting the vane zone, the fluids continued to flow along a skewed path to form a screw-like trajectory. Furthermore, the trajectory spiral varied with the distance from the vane zone. This is a result of the formation and decay of the swirling flow field, which will be discussed in detail in Sec. IV H. Under these conditions, due to the tremendous density variance between the gas and liquid phases, bubbles migrated to the pipe center in the radial direction under the effect of a centrifugal force. Subsequently, the

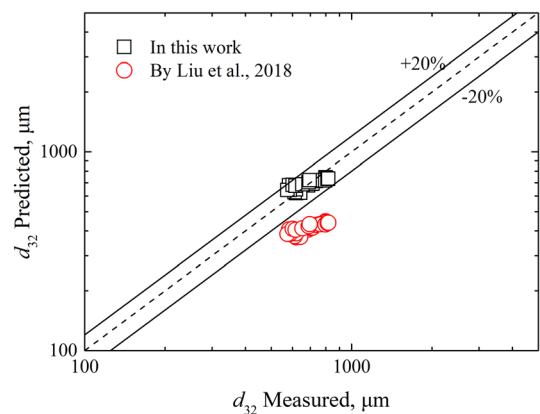


FIG. 5. Comparison of predicted *d*₃₂ vs measured *d*₃₂.

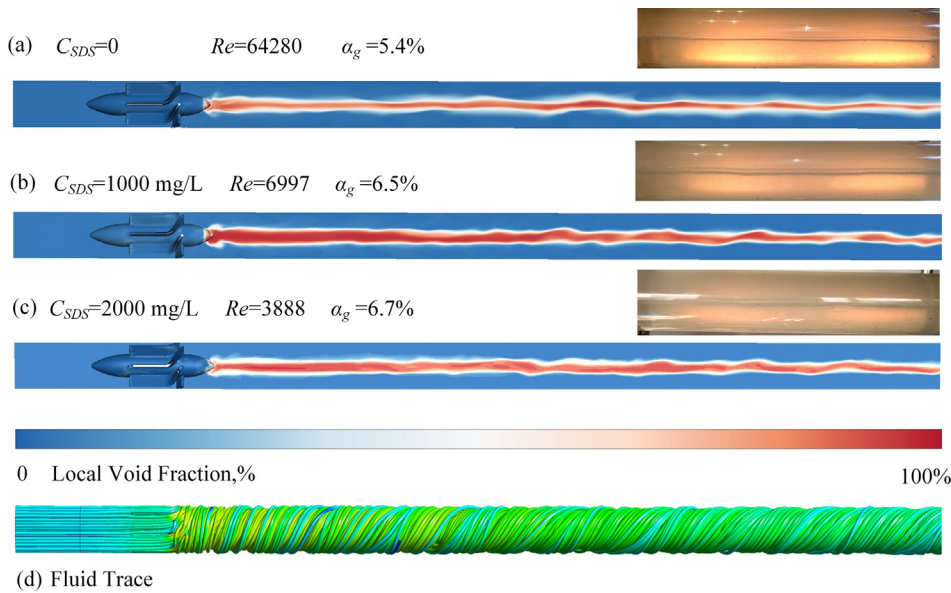


FIG. 6. Comparison of CFD and observation under different operating conditions [(a) $C_{SDS} = 0$, $Re = 64\,280$, $\alpha_g = 5.4\%$; (b) $C_{SDS} = 1000$ mg/l, $Re = 6997$, $\alpha_g = 6.5\%$; (c) $C_{SDS} = 2000$ mg/l, $Re = 3888$, $\alpha_g = 6.7\%$; (d) fluid trace].

bubbles merged rapidly and formed a continuous gas column. Comparing Figs. 6(a)–6(c), it is obvious that the gas column size changed with different Reynolds numbers and liquid rheology parameters. When the Reynolds number was large and the liquid viscosity was small, the gas column was as thin as a line. Meanwhile, under similar entrance conditions, the gas column became wider as the liquid phase was changed from water to SDS solution with a 1000 mg/l concentration. This can be attributed to dissipation variance induced by the viscosity in the fluid domain. When the pure water was changed to a shear-thinning power-law fluid, and the consistency k was $0.013\,37\text{ Pa s}^n$, the apparent viscosity increased along with the turbulence dissipation. Under such conditions, more energy remained in the form of potential energy and kinetic energy, which can be regarded as pressure and velocity. Moreover, considering the force balance at the gas–liquid interface, the gas column became wider as the liquid viscosity increased.

Figure 7 provides a comparison of the void fraction tomography from the CFD and ERT measurements in the testing section 6D downstream of the vane zone. The figure provides both contour comparisons and void fraction radial profile distributions. It can be seen that for the given operating parameters, the section void fraction contours obtained by ERT and CFD both showed gas columns in the pipe center with similar sizes, surrounding which there was a phase transition to pure liquid. As the resolution of ERT may be relatively low as the electrodes are limited, the transition may have a wider range than in the CFD case, but this has little influence on the overall discussion. As is shown in the plots, there were narrow amplitudes at the location $r/R = 0$, corresponding to a gas column in the contours. The void fraction curve amplitudes obtained by CFD were within the error range of the void fraction curve amplitudes obtained by ERT. Furthermore, the widths of the curves between the CFD and ERT measurements were similar.

Table II presents a further comparison between the CFD and experimental measurements from the perspective of the pressure drop.

It can be seen that despite the additional pressure drop induced by the pressure gauge testing section, the pure pressure drops for all the cases measured were larger than the simulation drops. This may result from an abrupt fluid domain change induced by a flange gasket used for connection or the sampling elbow to measure the entrance bubble size distribution. Nevertheless, the effect is tiny, with the relative deviations between the CFD and measurement being less than 7%. From the discussions above on both the void fraction distribution and pressure drop, it can be concluded that the CFD is reliable enough to describe the shear-thinning power-law gas–liquid swirling flow field.

C. Viscosity distribution

For shear-thinning power-law fluids, as the apparent viscosity is dependent on the n th power of the shear rate, a comprehensive understanding of the apparent viscosity distribution is beneficial for further discussion of the velocity distribution and swirl intensity decay. As the consistency k has a significant influence on the apparent viscosity μ_{app} , the apparent viscosity was normalized by a factor of $1/k$ to examine the influence of the index n . Figure 8 presents a normalized mixture viscosity distribution under a given consistency k . It is obvious that the μ_{app}/k was smaller than one for all of the cases recorded. Furthermore, the gas viscosity is tiny compared to the liquid viscosity and the gas column in the pipe center. A low viscosity column appears in correspondence with the gas column. Outside the column, the mixture viscosity is mainly dependent on the rheology of the liquid phase. As n was smaller than 1 for all of the cases in this work, the discrepancy between k and μ_{app} was larger with increasing shear rate. This can be related to the shear-thinning power-law properties when the index n is smaller than one. For Newtonian fluids, $n = 1$ with a power-law model, and the apparent viscosity is equal to k . The shear stress is in proportion to the shear rate. Under the $n < 1$ condition of shear-thinning fluids, the apparent viscosity is proportional to the $n-1$ th power of the shear rate, and the shear stress is proportional to the n th

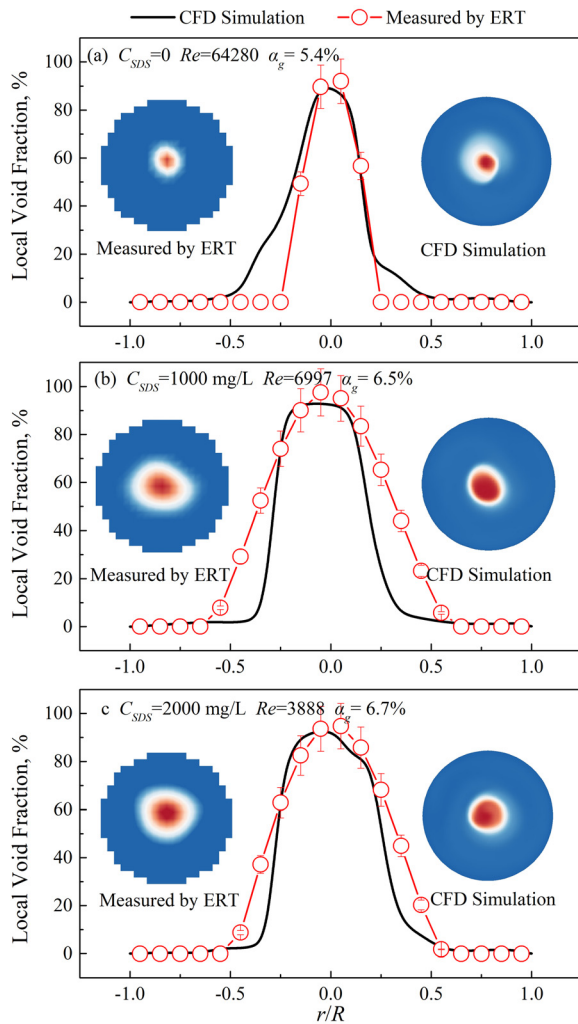


FIG. 7. Comparison of CFD and ERT measurement at section 6D downstream vane zone [(a) $C_{SDS} = 0$, $Re = 64\,280$, $\alpha_g = 5.4\%$; (b) $C_{SDS} = 1000$ mg/l, $Re = 6997$, $\alpha_g = 6.5\%$; (c) $C_{SDS} = 2000$ mg/l, $Re = 3888$, $\alpha_g = 6.7\%$].

power of the shear rate. When n is small enough to be approximately zero, the shear stress is approximately equal to k numerically, while the apparent viscosity is approximately in proportion to the reciprocal of the shear rate. Considering the shear rate is larger than 1 s^{-1} in this work, it is unsurprising that a smaller index n results in a larger

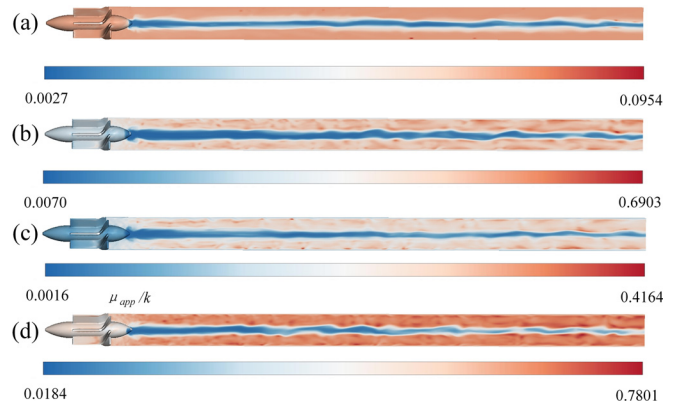


FIG. 8. The contour of μ_{app}/k distribution under variant rheology parameters [(a) $k = 0.01337\text{ Pa s}^n$, $n = 0.08056$; (b) $k = 0.01337\text{ Pa s}^n$, $n = 0.80557$; (c) $k = 0.02\text{ Pa s}^n$, $n = 0.65$; (d) $k = 0.02\text{ Pa s}^n$, $n = 0.89$].

discrepancy between μ_{app} and k . A narrower μ_{app}/k range in the contours consequently appears.

The discussions above can explain the uniformity variance of the μ_{app}/k contours as well. Though the μ_{app}/k contours in all cases were within relatively large ranges from 10^{-3} to the maximum amplitude, most of the fluid domain μ_{app}/k values occupied a narrow band in the color map. A small μ_{app}/k value variance appeared due to turbulent fluctuations, inducing a discrepancy in the uniformity. However, as n decreased, the discrepancy in the uniformity was reduced to give nearly evenly distributed μ_{app}/k outside the gas column when n was smaller than 0.1. This is in accordance with the discussion above. As n gradually approached zero, the shear stress became uniform, while μ_{app} approached the reciprocal of the shear rate. Moreover, as the viscosity became smaller, the related energy dissipation decreased, leaving a larger velocity and a more evenly distributed shear rate. Consequently, the apparent viscosity uniformity of the mixture was increased.

D. Gas-phase distribution

The void fraction distribution is one of the parameters of significance in gas–liquid swirling flow fields. Figure 9 presents the iso-surface of the gas column in the downstream vane zone with different liquids and Reynolds numbers. The gas column is similar to CFD obtained by Yin of Newtonian gas–liquid swirl flows.³³ For the cases recorded, the entrance gas volume fractions were around 6%, whereas the liquid rheology parameter varied, resulting in distinct Reynolds numbers. As is shown in Figs. 9(a) and 9(b), when the consistency k

TABLE II. Comparison between measurement and simulation.

Case No.	SDS Concentration mg/l	Inlet flow rate (m ³ /h)	Re	Gas concentration (%)	Power-law fluid parameter		Pressure drop (Pa)	
					k (Pa s ⁿ)	n	Measurement	Simulation
1	0	18.2	64280	5.4	0.00100	1.00000	2205.2	2056.4
2	1000	18.4	6997	6.5	0.01337	0.80557	2296.9	2176.8
3	2000	16.5	3888	6.7	0.02721	0.66209	1792.7	1727.4



FIG. 9. Gas column distribution under different fluid rheology parameters [(a) $k = 0.01337 \text{ Pa s}^n$, $n = 0.08056$, $\alpha_{giso} = 0.8$, $Re = 25447$; (b) $k = 0.01337 \text{ Pa s}^n$, $n = 0.80557$, $\alpha_{giso} = 0.8$, $Re = 6997$; (c) $n = 0.02 \text{ Pa s}^n$, $n = 0.65$, $\alpha_{giso} = 0.65$, $Re = 5836$; (d) $k = 0.02 \text{ Pa s}^n$, $n = 0.89$, $\alpha_{giso} = 0.65$, $Re = 3732$; and (e) pure water, $\alpha_{giso} = 0.65$, $Re = 64280$].

was 0.01337 Pa s^n , the gas column width varied with index n . The larger the index n , the wider the gas column. The same goes for the condition when k was 0.02 in Figs. 9(c) and 9(d). Another obvious trend is that when n was large, the iso-surface of the void fraction was more distorted, like a ribbon rather than a column. When the liquid was changed to pure water, the gas column was reshaped into an ideal cylinder. The variation of the gas column size and shape is sensitive to the Reynolds number and Weber number, meaning the interaction of the viscous force and surface tension force. When the Reynolds number is large enough, the inertial force is dominant over the viscous force, as well as the shearing effect of the liquid phase near the gas–liquid interface. Under such conditions, together with the interactive mechanism model proposed in our previous work, the gas column can maintain a relatively thin size.⁹ Furthermore, with a smaller length scale, the Weber number is small, resulting in a larger surface tension force than inertial force. This means the gas column can resist the turbulent shearing of the liquid phase and can maintain a small radius without meaningful distortion by the surrounding shearing. On the contrary, when k or n is increased, a smaller Reynolds number reflects a weaker inertial force effect, and the gas column size is increased due to the balancing of the inertial force, the surface tension force, and the viscous force. A smaller surface tension force induced by a larger gas column makes the gas column too weak to resist surrounding shearing without distortion. Consequently, the gas column is twisted and distorted.

E. Fluid domain pressure distribution

The pressure drop is a fluid domain parameter relevant to further applications and fluid–structure optimization. In this subsection, the pressure drop is normalized by a factor of $1/2\rho U_0^2$ to obtain the Euler number, Eu . Figure 10 shows the normalized pressure drop along the axial flow direction under conditions with various liquid rheology parameters. Eu is a relative value based on the average outlet pressure. For all cases recorded, Eu decreased abruptly in the vane zone as the hub occupied the original flow area and accelerated the fluids, inducing a larger pressure drop. Downstream of the vane zone, as the hub tail appeared, the flow area increased to the original pipe cross-section area. Hence, the local velocity decreased and the Eu curve showed a small peak, before gradually decaying until the exit. As is shown in

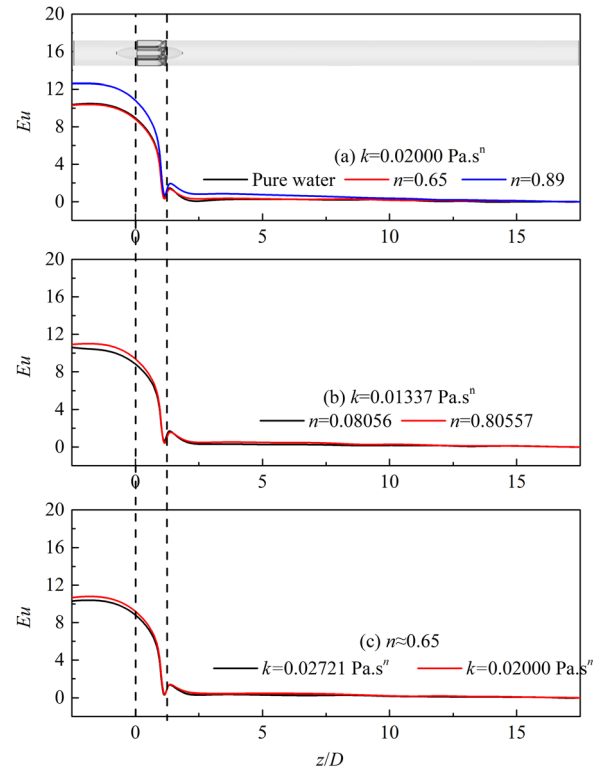


FIG. 10. Normalized pressure drop along the flow direction with a variation of rheology parameters [(a) $k = 0.02000 \text{ Pa s}^n$; (b) $k = 0.01337 \text{ Pa s}^n$; and (c) $n \approx 0.65$].

Figs. 10(a) and 10(b), when the consistency k was fixed, the Eu value increased with increasing index n . As discussed in the subsections above, increasing the index n resulted in a lower Reynolds number, increasing the viscous force. Under such conditions, the energy dissipation viscously enlarged considerably, and the pressure drop increased over fixed axial distances. Hence, the curve value increased. The same goes for the consistency k . As k increased in Fig. 10(c), the apparent viscosity increased. As a consequence, the Reynolds number decreased and the viscous energy decay increased. Hence, Eu with a larger consistency k was larger than that for a smaller k . For Fig. 10(a), which shows the curves for pure water and $n = 0.65$ (operating case 6), the curves showed a little discrepancy. This is because of the counteracting effects of a larger consistency k enhancing the viscous decay while a smaller index n reduced it. As a consequence, the two Eu curves are very similar.

The section pressure distribution plays an important role in the formation of a gas column. Figure 11 illustrates the radial pressure variance for different cases $9D$ downstream of the cross section. The pressure was normalized to Eu to exclude the influence of the density and velocity. For all cases, the Eu valley appeared in the pipe center zone. The pressure gradually increased as r/R increased from 0 to 1. The gas–liquid interface was located around the valley region. With the disturbance of the column, the section Eu profile sometimes showed a tiny asymmetry. Fixing the consistency k and changing the index n , as shown in Figs. 11(a) and 11(b), the Eu value with a smaller index n is almost larger than the Eu value with a larger index n for all radial

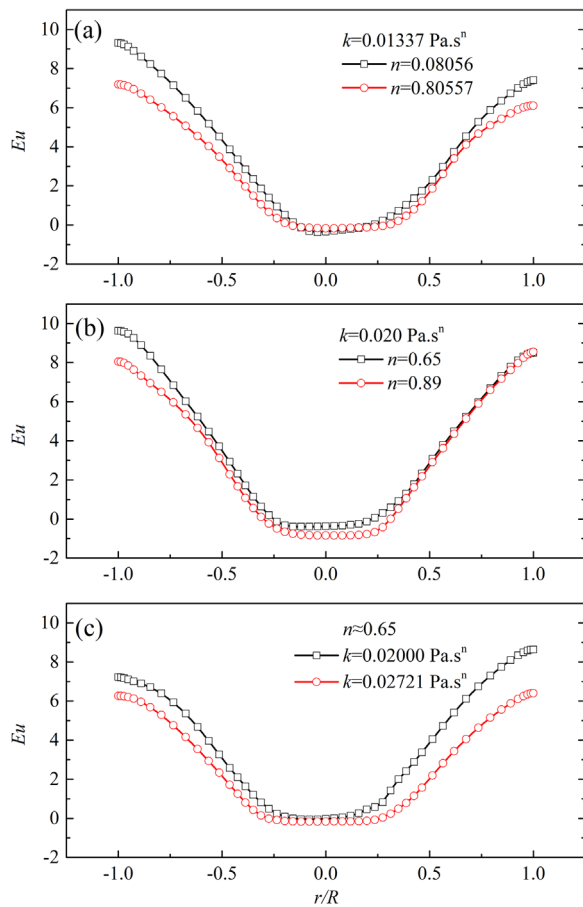


FIG. 11. Normalized pressure distribution in the radial direction at section 9D downstream vane [(a) $k = 0.01337 \text{ Pa}\cdot\text{s}^n$; (b) $k = 0.020 \text{ Pa}\cdot\text{s}^n$; and (c) $n \approx 0.65$].

locations. Furthermore, curves with smaller index n were steeper and showed a larger Eu variation range than those with larger n . The same goes for the trends of consistency k . Increasing these parameters reduced the Reynolds number for given entrance operating parameters. As a consequence, the viscous force increased, enlarging the turbulent viscous decay, as expected. In the radial direction, the radial velocity u_r is far less than u_t . By ignoring u_r and the variation with θ by considering circumferential symmetry, the time-averaged N–S equation in the radial direction can be simplified. The partial derivative of p with respect to r is only related to $u_t^2/\rho r$. When normalized, it becomes a partial derivative of p^* with the r^* profile sensitive to u_t^{*2}/r^* and in which p^* can be regarded as Eu . Consequently, as k or n increased, the viscous decay increased, and the tangential velocity u_t decreased. Thus, the gradient of the Eu profile decreased. Furthermore, as the decay increased, the remaining pressure decreased, so the Eu profile was lower.

Figure 12 shows the Eu variation along the axial direction for selected cases. Being similar to results obtained by the Slot of the oil–water swirling flow, the curve slope gradually decreased downstream.¹⁸ In other words, the Eu profiles were smoother, which is expected. As discussed above, the Eu profile slope is sensitive to the

tangential velocity. As the tangential velocity decays along the flow, u_t^{*2}/r^* is gradually reduced. It is unsurprising that the Eu profile becomes smoother. When the liquid rheology parameter is changed, if the variation of k and n reduces the Reynolds number, the decay of the tangential velocity is more apparent. Consequently, the profile gradient variation will be more obvious, as shown in the comparison between Figs. 12(a) and 12(b). It further means less body rotation of the core region according to the slot.¹⁸

F. Tangential velocity distribution

Figure 13 shows the cross-sectional normalized tangential velocity distribution along the swirling flow field for different fluid rheology parameters. It is obvious that near the vane zone, the distribution of the tangential velocity was not regular as the swirling flow domain was still forming. In the downstream development period, regular distributed tangential velocity sections appeared and the tangential velocity decayed. For a given cross-section in the decaying section, the pipe center suffered from a low-velocity magnitude. Outside the pipe center, a ring zone with a large tangential velocity appeared. Furthermore, on approaching the wall, the tangential velocity decreased to zero. Another obvious phenomenon was that as the fluid flowed downstream, the tangential velocity peak value in the contour gradually decayed. This is in agreement with an observation presented by Kitoh.¹ Furthermore, when the fluid rheology parameter and entrance conditions changed, the normalized sectional tangential velocity magnitude changed as well. Comparing Figs. 13(a) and 12(b), it is obvious that as index n decreased, more sections showed a dimensionless tangential velocity contour with a high peak value. The tangential velocity decayed more slowly along the axial direction. Comparing Figs. 13(b) and 13(c), it can be seen that as the consistency k increased, the tangential velocity decayed more quickly along the axial direction. The phenomena above concern the Reynolds number variation induced by the liquid rheology parameters. As the Reynolds number decreased because of k or n , the viscous dissipation on the tangential momentum increased, leaving less tangential momentum, which was related to the tangential velocity.

Figure 14 presents a dimensionless tangential velocity profile in the radial direction. Figure 14(a) compares the normalized tangential velocity from the CFD with the experimental data from Kitoh for a swirling number of 1.0 for pure water.¹ It can be seen that the CFD and measurement profiles had the same peak value at similar r/R locations. This can be regarded as a division point between the core region and the annulus region. Inside the core region, the tangential velocity increased from almost zero to the peak value monotonically, which is similar to a forced vortex, while outside in the annulus region, the tangential velocity decreased slowly and showed an abrupt reduction to zero near the wall. The overall velocity profiles from the CFD and Kitoh were similar to Rankine vortices in viscous fluids.¹³ Tiny discrepancies are seen between the CFD results and Kitoh’s data. This results from the fact that the CFD includes a 5.4% gas fraction, which may compress the tangential velocity profile in the wall direction, and the difference in the overall history of the core region.¹ Nevertheless, these discrepancies are tiny, so the CFD results can be considered validated by the measured data. Figures 14(b)–14(d) compares the normalized tangential velocity profiles with various liquid rheology parameters. It is obvious that with the reduction in the consistency k and index n , the

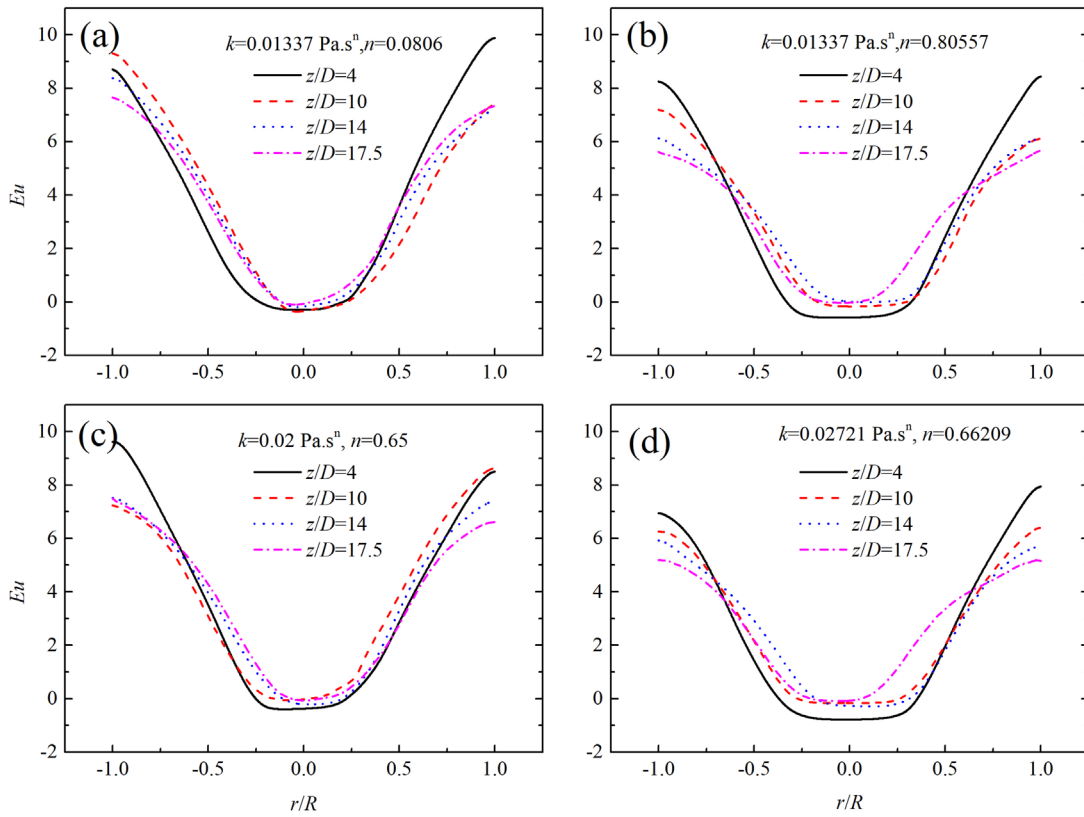


FIG. 12. Normalized pressure distribution along the flow direction [(a) $k = 0.01337 \text{ Pa s}^n$, $n = 0.0806$; (b) $k = 0.01337 \text{ Pa s}^n$, $n = 0.80557$; (c) $k = 0.02 \text{ Pa s}^n$, $n = 0.65$; and (d) $k = 0.02721 \text{ Pa s}^n$, $n = 0.66209$].

velocity profiles both increased. This can be explained by the Reynolds number variation discussed above.

Figure 14 further shows the normalized tangential velocity variation along the axial flow direction. When z/D was 4, $3D$ downstream of the vane zone, the tangential velocity magnitude was large. Subsequently, with the increases in the axial distance from the vane zone, the tangential velocity magnitude kept decaying and the division point of the core region and the annulus region gradually moved

toward the pipe center, causing a decaying “forced vortex” zone. These phenomena reflect the reduction of the tangential momentum flux in the axial direction and are in coincidence with CFD and measurement data presented by Slot and Dirkszwaiger.^{16,37} Furthermore, as n or k increased, the reduction was more obvious, as can be seen by comparing Figs. 15(a) and 15(b), or 15(b) and 15(d). This was closely related to the interaction between the inertial force and the viscous force characterized by the Reynolds number. The reduction of the Reynolds

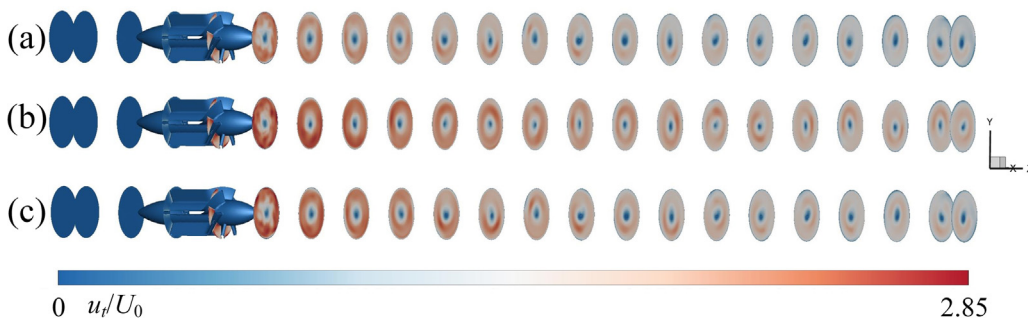


FIG. 13. Normalized tangential velocity distribution along the axial direction [(a) $k = 0.02 \text{ Pa s}^n$, $n = 0.89$, $Re = 2723$; (b) $k = 0.02 \text{ Pa s}^n$, $n = 0.65$, $Re = 5836$; and (c) $k = 0.02721 \text{ Pa s}^n$, $n = 0.66209$, $Re = 3888$].

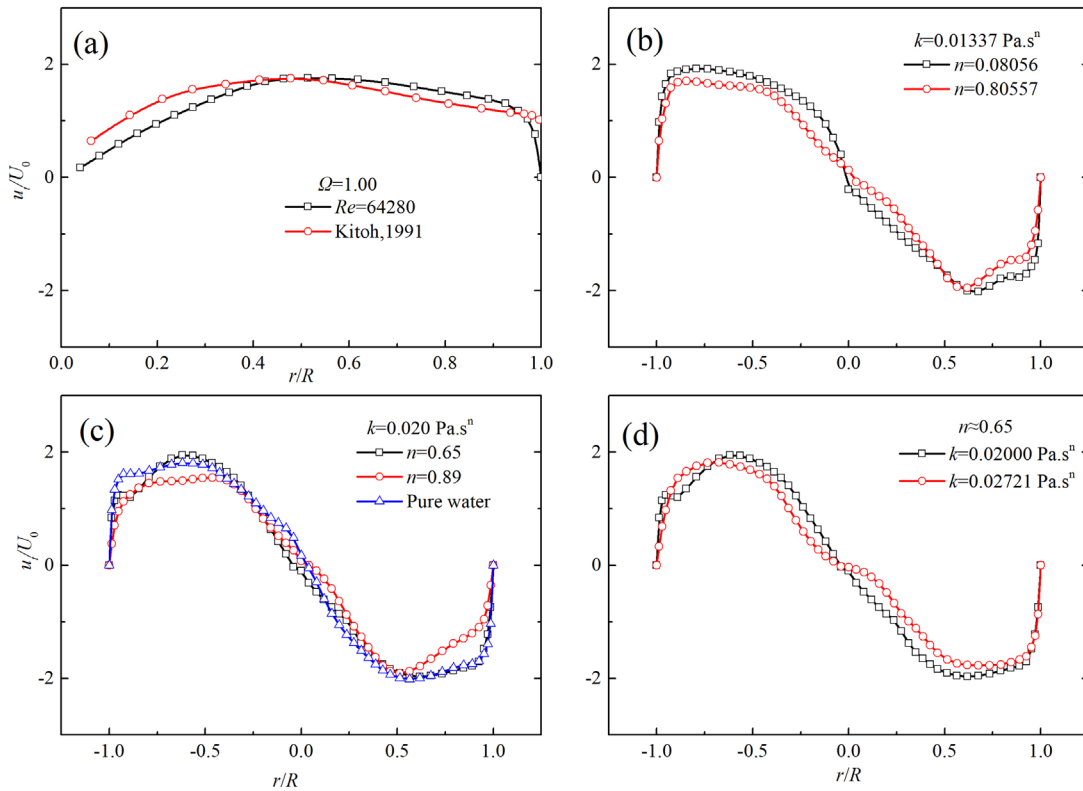


FIG. 14. Normalized tangential velocity distribution in the radial direction at section 9D downstream vane [(a) data by Kitoh vs $Re = 64\,280$; (b) $k = 0.013\,37\text{ Pa}\cdot\text{s}^n$; and (c) $k = 0.020\text{ Pa}\cdot\text{s}^n$; d. $n \approx 0.65$].

number meant a stronger viscous dissipation of the tangential flux momentum, resulting in a lower tangential velocity magnitude and a smaller core region range.

G. Axial velocity distribution

Figure 16 shows a normalized axial velocity contour along the axial direction under various liquid rheology parameters. The axial velocity distribution was not distributed regularly when the fluids flowed out of the vane zone. A longitudinal developing section was needed. Downstream of the developing section, the distribution of the axial velocity was relatively regular and gradually became uniform, in what can be called the decaying part. In this part, for a given cross section, the pipe center suffered from a low axial velocity value. Outside the pipe center, the axial velocity gradually increased to its peak value, then decreased slowly until the wall region in which a sudden decrease occurred. As the fluid flowed along the axial direction, the sectional peak value gradually decayed, especially for larger k and n values. Under such conditions, as is shown in Figs. 16(b) and 16(c), as the Reynolds number decreased, the section uniform distribution axial velocity trend was more obvious under larger k or n . As was discussed above, when the Reynolds number decreased, the viscous force increased compared with the inertial force. Under such conditions, the decay of the tangential velocity was more significant within a fixed axial distance. The axial velocity redistribution uniformly trends

occupied more predominance. Consequently, the sectional axial velocity became more uniform. Furthermore, under similar Reynolds numbers, a larger index n better promoted the sectional axial velocity to distribute it more uniformly. This is expected. A change in the consistency k influences the stress tensor as a scale factor of the whole fluid domain, while the influence of the index n is in relation to the strain tensor, which varies according to the location in the swirling location.

The trends above become more obvious for the radial axial velocity profiles. Figure 16 presents the radial axial velocity profiles 9D downstream of the vane zone under various liquid rheology parameter conditions. Clearly, the axial velocity in the pipe center was small. Subsequently, the axial velocity gradually increased to a maximum and suffered from an abrupt decrease in the near-wall zone. When index n decreased, as shown in Figs. 17(a) and 17(b), the amplitude increased. Meanwhile, an increment in consistency k induced a reduction in the amplitude when the index n was kept almost constant.

Figure 18 further presents the variation of the normalized axial velocity along the axial direction under variant liquid rheology parameter conditions. For all cases recorded, the axial velocity showed a similar profile with a low value in the pipe center. Irregularities could appear as the influence of instant fluctuations induced by gas–liquid surface changes and gravity. Nevertheless, the overall trend is obvious. The non-uniformity of the velocity profile gradually decayed along the axial direction, reflecting the decay of the tangential momentum, which shows coincidence trends with the observation proposed by

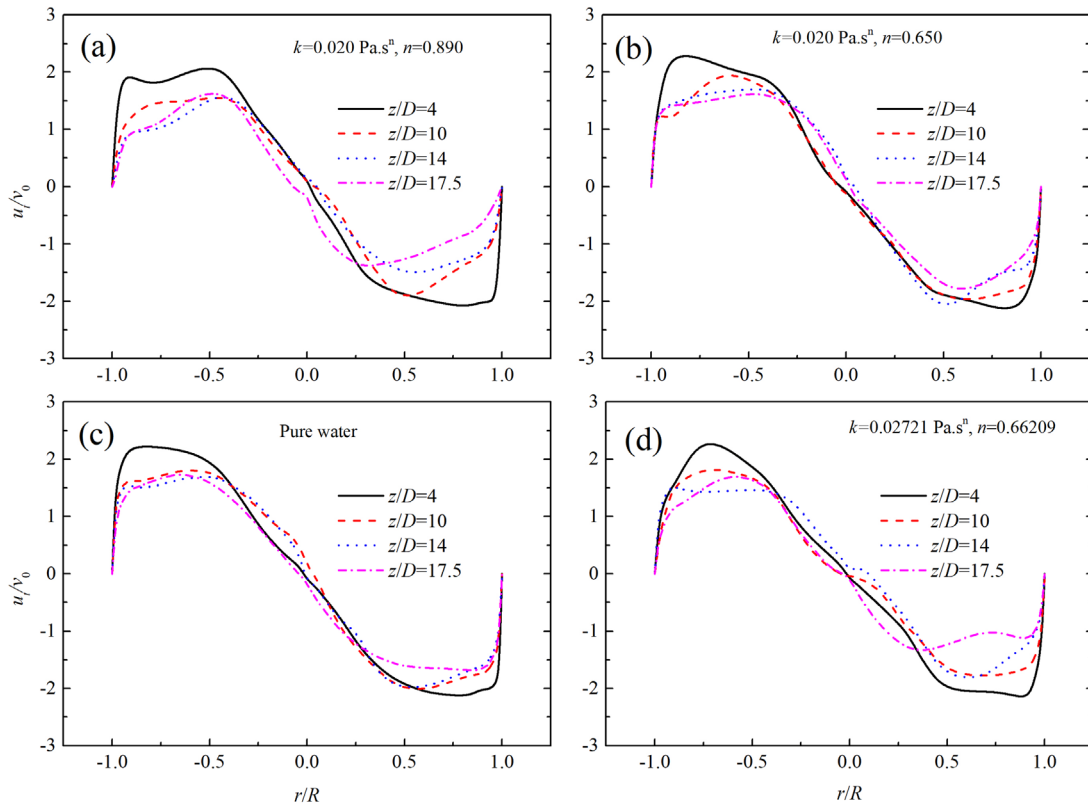


FIG. 15. Dimensionless tangential velocity distribution radially along the flow direction [(a) $k = 0.020 \text{ Pa s}^n$, $n = 0.890$; (b) $k = 0.020 \text{ Pa s}^n$, $n = 0.650$; (c) pure water; and (d) $k = 0.02721 \text{ Pa s}^n$, $n = 0.66209$].

Kitoh.¹ When z/D was 4, 3D downstream of the vane zone, reverse flow was observed in all cases as presented by Cai *et al.*⁶ As the tangential momentum attenuated, the axial reverse flow gradually disappeared, and the axial velocity at the pipe center increased while the peak value in the profile decreased, making the axial velocity more uniformly distributed. Furthermore, 20 times as pure water of consistency k was in value, axial velocity uniformity along the axial direction was more obvious [Figs. 18(a), 18(b), and 18(d)]. In addition, a larger

index n would aggravate this phenomenon as it weakens the liquid shear thinning properties.

H. Swirl intensity decay

Tangential momentum flux is one of the unique characteristics of a swirling flow field. The swirl intensity can be expressed by the dimensionless number Swirl number Ω . Several forms of the Swirl

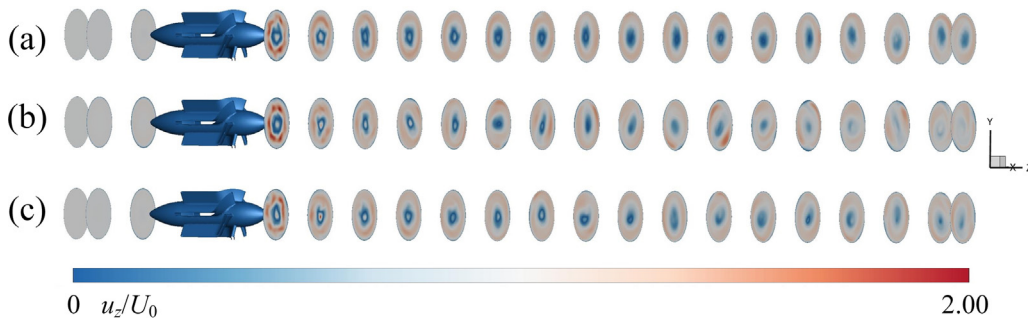


FIG. 16. Normalized axial velocity distribution along the axial direction [(a) $k = 0.02 \text{ Pa s}^n$, $n = 0.65$, $Re = 5836$; (b) $k = 0.02 \text{ Pa s}^n$, $n = 0.89$, $Re = 3732$; and (c) $k = 0.02721 \text{ Pa s}^n$, $n = 0.66209$, $Re = 3888$].

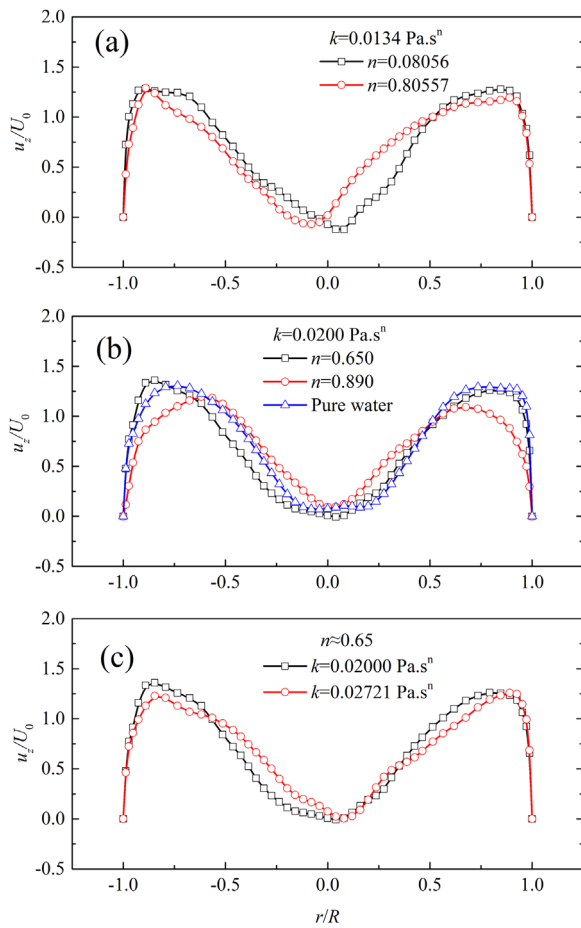


FIG. 17. Normalized axial velocity distribution in the radial direction at section 9D downstream vane [(a) $k = 0.134 \text{ Pa s}^n$; (b) $k = 0.020 \text{ Pa s}^n$; and (c) $n \approx 0.65$].

intensity have been applied. For instance, Kitoh defined the swirl number Ω_o in the form of the equation below:¹

$$\Omega_o = 2\pi\rho \int_0^R u_t u_z r^2 dr / \rho\pi R^3 U_0^2. \quad (22)$$

Following Kitoh’s definition of the Swirl number, the gas–water swirl intensity obtained by CFD in this work was compared with Kitoh’s measurements. As is shown in Fig. 19(a), the swirl number from the CFD and the measured data from Kitoh were compared in a logarithmic coordinate system. As has been observed by multiple researchers, the swirl intensity of the pure water in the CFD case decayed with an exponential behavior with linear regularity appearing in the logarithmic coordinate system.¹ Furthermore, the slope of the pure water case in this work was similar to that of data obtained by Kitoh, with the variance in the intercepts resulting from the vortex-inducing method, the initial swirling intensity, and the small influence of the gas phase. Nevertheless, the decaying law was constant once the fluid type was given and was in the decaying section.

Several other forms for the swirl number have also been proposed. Among these, the ratio of the tangential momentum flux to the

axial momentum flux in the axial direction is always applied.⁹ For a gas–liquid two-phase flow, Ω can be expressed as follows in accordance with our previous works:^{4,9}

$$\Omega = \frac{1}{R} \frac{\int_0^R (\alpha_l \rho_l u_{lt} u_{lz} + \alpha_g \rho_g u_{gt} u_{gz}) r^2 dr}{\int_0^R (\alpha_l \rho_l u_{lz}^2 + \alpha_g \rho_g u_{gz}^2) r dr}, \quad (23)$$

where R is the radius of the fluid domain, subscript g refers to the gas phase, subscript l refers to the liquid phase, u_t is the tangential velocity, and u_z is the axial velocity. Figures 19(b)–19(d) shows the variation in the Swirl number Ω along the flow direction under various liquid rheology parameter conditions. The curve can be divided into developing sections and decaying sections. The developing section was the section where the swirl flow formed after exiting the vane zone until the swirl number reached its maximum value, while the decaying section refers to the section where the swirl strength decayed.

The length and peak value of the developing section varied with the liquid rheology parameters. As was seen in our previous study, the length and peak value of the developing section are sensitive to the gas void fraction. A longer distance was needed with a larger void fraction and a smaller Reynolds number when the liquid phase was pure water.^{4,9} The liquid power-law parameters had an effect on the peak value and the length of the developing section as well. It can be seen that the index n mainly influenced the developing length while the consistency k mainly had an effect on the peak value. A smaller index n shortened the developing length as it compressed the stress tensor variation range to make the fluid thinner, forming a fully developed vortex at a shorter distance. In comparison, a larger consistency k enlarged the stress tensor as well as the viscous dissipation. Under such conditions, a lower percentage of tangential momentum remained when the vortex was fully formed, with a lower swirl number peak value appearing as consequence.

In the decaying section, the swirl number showed an exponential relationship with z/D . The exponential decay profiles were sensitive to liquid rheology parameters. As illustrated in Figs. 19(b)–19(d), the profile can be expressed as Eq. (24),

$$\Omega = A \cdot \exp(B \cdot z/D), \quad (24)$$

where A and B are parameters sensitive to Re , α_g , the consistency k , and index n . Similar decay regular can be seen in laminar and turbulent swirl flow with Newtonian liquids.^{1,13,14} In laminar swirl flows, Beaubert proposed tangential velocity in the form of Eq. (25) and axial velocity in the form of Eq. (26),¹⁴

$$u_t = u_{tmax} \varphi(r) \exp(\alpha \cdot z/D), \quad (25)$$

$$u_z = u_0 \left(1 - \frac{r^2}{R^2} \right), \quad (26)$$

in which u_{tmax} is the maximum tangential velocity, $\varphi(r)$ is the dimensionless tangential velocity profile, and α is a dimensionless scaling parameter. When the deducting swirl number following Eq. (23) and integrating components with r , a component with $\exp(\alpha \cdot z/D)$ can be found, which is similar to Eq. (25), whereas in turbulent swirl flows, Kitoh proposed a co-relationship of wall shear stress with swirl intensity and found exponential swirl decay along the pipe axial direction.

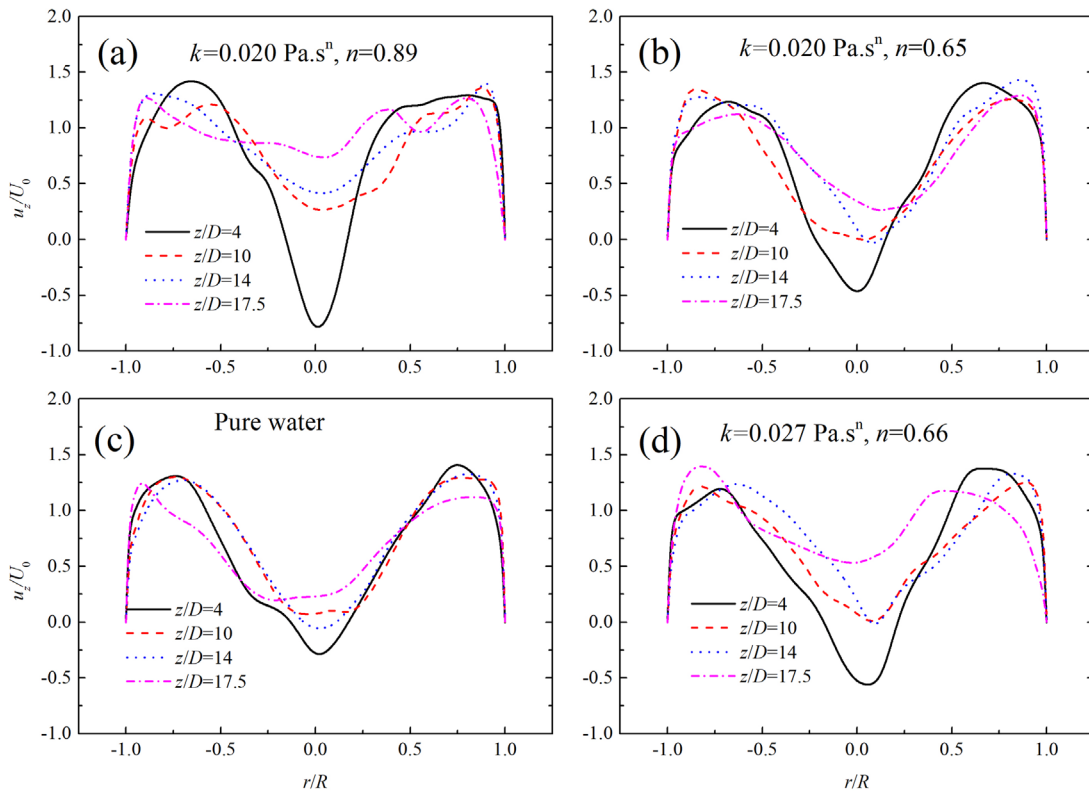


FIG. 18. Normalized axial velocity distribution radially along the flow direction (a) $k=0.020 \text{ Pa s}^n$, $n=0.89$; (b) $k=0.020 \text{ Pa s}^n$, $n=0.65$; (c) pure water; and (d) $k=0.027 \text{ Pa s}^n$, $n=0.66$].

In fact, tangential momentum gradually dissipates due to stress tensor. The slope parameter B quantifies the percentage of tangential momentum dissipated in the fixed uniformed axial distance. It is a parameter in deep relation with viscosity according to Beaubert in laminar Newtonian swirl flows and can be regarded as tangential momentum attenuation speed in the axial direction.¹⁴ In this work, the consistency k and index n influence Reynolds number and apparent viscosity as well, which further determines Reynolds number and shear stress. A larger index n and consistency k enlarge shear stress in exponentially and linearly behavior respectively. All these increments induce a larger percentage of swirl intensity dissipation in the fixed axial distance (z/D), which is corresponded with the larger absolute value of B presented in Fig. 19.

Furthermore, parameter A in Eq. (24) reflects swirl flow formation history. It can be regarded as initial swirl intensity, which is sensitive to vane zone geometry configuration and fluid rheology properties. As the vane zone geometry configuration is fixed, larger consistency k and index n bring additional tangential momentum dissipation in the developing section, and smaller initial swirl number Ω appears as a consequence and induces smaller parameter A .

V. CONCLUSION

To investigate a gas–liquid swirling flow with shear-thinning liquid, this work has presented a dimensional analysis to find out the key dimensionless parameters. Concentrating on the key dimensionless

parameters above, experimental measurements and CFD simulations were conducted. The Malvern particle size analyzer and ERT were applied to measure the entrance bubble size and cross-sectional void fraction, respectively. Validated by measurements, the mixture multi-phase model coupled with the large eddy simulation turbulence model was applied in CFD to further reveal the gas–liquid swirling flow properties, including the void fraction, pressure, velocity, and swirl intensity.

The fluid domain can be divided into a developing section and a decaying section in the axial direction for a vane-type swirling flow field. The tangential momentum induces a core-annulus flow structure in the gas–liquid swirling flow. A reduction in the shear-thinning power-law index n of the liquid phase constrains the stress tensor by modifying the power index in the apparent viscosity. Thus it causes the swirl flow to form over a shorter distance with a stronger swirl intensity and helps the development of the core-annulus flow structure. Under such conditions, the flow decays slowly and the gas core becomes thinner in size. However, an increment in the consistency k enlarges the stress tensor proportionally. The swirl flow structure forms with a weaker swirl intensity. The core-annulus flow structure exhibits a smaller pressure and velocity amplitude. As a consequence, the tangential momentum decay is aggravated and the gas core width increases as well.

In the decaying section, the swirl intensity decays in the exponential form, and the parameters of the exponential relationship are

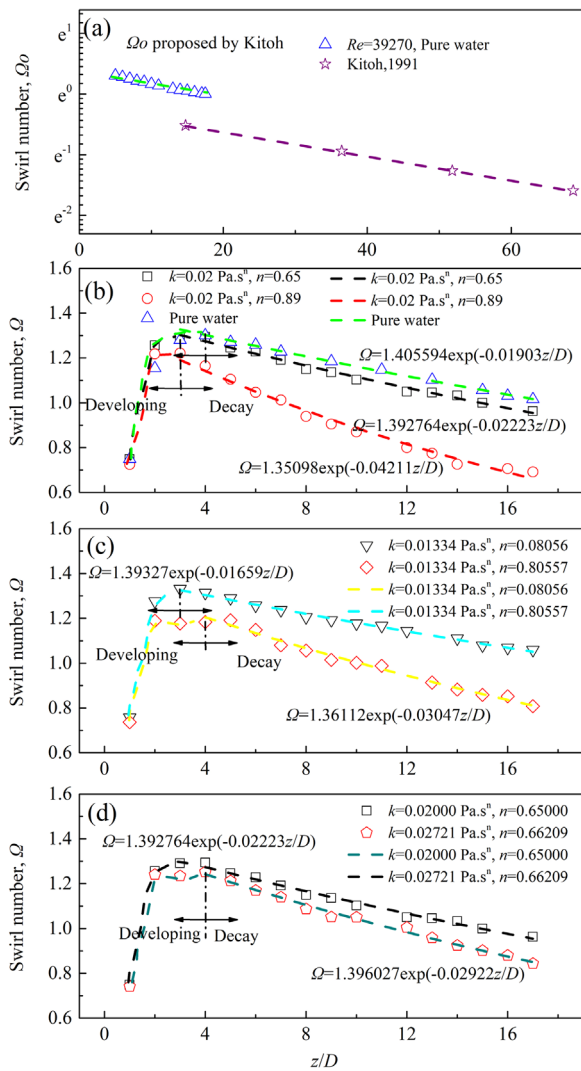


FIG. 19. Swirl intensity variation under different rheology parameter conditions [(a) pure water, $Re = 39270$ vs data by Kitoh; (b) $k = 0.02 \text{ Pa s}^n$; (c) $k = 0.01334 \text{ Pa s}^n$; and (d) $k = 0.2000 \text{ Pa s}^n$, $n = 0.65$, vs $k = 0.02721 \text{ Pa s}^n$, $n = 0.66209$].

sensitive to the consistency k and index n in the cases recorded. Increases in k and n induce a smaller initial swirl intensity and steeper exponential slope as they enlarge the stress tensor together. Findings in this work are beneficial for gas–liquid separator design and optimization when processing gas–liquid mixture with shearing thinning power-law liquids in the petroleum industry and other related fields.

ACKNOWLEDGMENTS

This work was supported by the National Natural Science Foundation of China (Grant No. 12102436) and the Strategic Priority Research Program of the Chinese Academy of Science (Grant No. XDB22030101).

AUTHOR DECLARATIONS

Conflict of Interest

The authors have no conflicts to disclose.

Author Contributions

Shuo Liu: Funding acquisition (equal); Investigation (equal); Writing – original draft (equal). **Jian Zhang:** Data curation (equal); Investigation (equal). **Jing-yu Xu:** Conceptualization (equal); Funding acquisition (equal); Project administration (equal).

DATA AVAILABILITY

The data that support the findings of this study are available from the corresponding author upon reasonable request.

REFERENCES

- ¹O. Kitoh, “Experimental study of turbulent swirling flow in a straight pipe,” *J. Fluid Mech.* **225**, 445–479 (1991).
- ²E. Laurila, D. Izbassarov, M. Järvinen, and V. Vuorinen, “Numerical study of bubbly flow in a swirl atomizer,” *Phys. Fluids* **32**(12), 122104 (2020).
- ³F. Seibold, P. Ligrani, and B. Weigand, “Flow and heat transfer in swirl tubes—A review,” *Int. J. Heat Mass Transfer* **187**, 122455 (2022).
- ⁴S. Liu, D. Zhang, L. L. Yang, and J. Y. Xu, “Separation characteristics of the gas and liquid phases in a vane-type swirling flow field,” *Int. J. Multiphase Flow* **107**, 131–145 (2018).
- ⁵J. Meng, F. Liang, S. Wang, and Z. He, “Experimental investigation of horizontal gas–liquid swirling flow characteristics using dual wire-mesh sensors,” *Int. J. Multiphase Flow* **149**, 103971 (2022).
- ⁶B. Cai, J. Wang, L. Sun, N. Zhang, and C. Yan, “Experimental study and numerical optimization on a vane-type separator for bubble separation in TMSR,” *Prog. Nucl. Energy* **74**, 1–13 (2014).
- ⁷W. Liu, K. Wang, and B. F. Bai, “Experimental study on flow patterns and transition criteria for vertical swirling gas–liquid flow,” *Int. J. Multiphase Flow* **122**, 103113 (2020).
- ⁸L. Liu, J. R. Zhang, S. Liu, K. Wang, and H. Y. Gu, “Decay law and swirl length of swirling gas–liquid flow in a vertical pipe,” *Int. J. Multiphase Flow* **137**, 103570 (2021).
- ⁹S. Liu, J. Zhang, L. S. Wang, and J. Y. Xu, “Separation mechanism and influential factor study on vane-type-associated petroleum gas separator,” *Sep. Purif. Technol.* **250**, 117274 (2020).
- ¹⁰J. J. Li, Y. L. Qian, J. L. Yin, H. Li, W. Liu, and D. Z. Wang, “Large eddy simulation of unsteady flow in gas–liquid separator applied in thorium molten salt reactor,” *Nucl. Sci. Tech.* **29**, 62 (2018).
- ¹¹P. Wei, D. Wang, P. Niu, C. K. Pang, and M. Liu, “A novel centrifugal gas liquid pipe separator for high velocity wet gas separation,” *Int. J. Multiphase Flow* **124**, 103190 (2020).
- ¹²L. Talon, “On the statistical properties of fluid flows with transitional power-law rheology in heterogeneous porous media,” *J. Non-Newtonian Fluid* **304**, 104789 (2022).
- ¹³G. K. Batchelor, “Axial flow in trailing line vortices,” *J. Fluid Mech.* **20**, 645–658 (1964).
- ¹⁴M. S. Uberoi, B. K. Shivamoggi, and S. S. Chen, “Axial flow in trailing line vortices,” *Phys. Fluids* **22**, 214–217 (1979).
- ¹⁵F. Beaubert, H. Pålsson, S. Lalot, I. Choquet, and H. Bauduin, “Fundamental mode of freely decaying laminar swirling flows,” *Appl. Math. Model.* **40**, 6218–6233 (2016).
- ¹⁶S. Y. Shi, J. Y. Xu, H. Q. Sun, J. Zhang, D. H. Li, and Y. X. Wu, “Experimental study of a vane-type pipe separator for oil–water separation,” *Chem. Eng. Res. Des.* **90**, 1652–1659 (2012).
- ¹⁷G. Vignat, D. Durox, and S. Candel, “The suitability of different swirl number definitions for describing swirl flows: Accurate, common and (over-) simplified formulations,” *Prog. Energy Combust. Sci.* **89**, 100969 (2022).

Downloaded from http://pubs.aip.org/journal/phf/article-pdf/doi/10.1063/5.0099895/16643118/073320_1_online.pdf

- ¹⁸J. J. Slot, "Development of a centrifugal in-line separator for oil–water flows," M.S. thesis (University of Twente, Dutch, 2013).
- ¹⁹Y. Chen, J. Luo, F. Wu, Z. Zhang, Z. Zhao, L. Zhang, C. Luo, and X. Li, "Multi-objective optimization on flow characteristics of pressure swirl nozzle: A LES-VOF simulation," *Int. Commun. Heat Mass Transfer* **133**, 105926 (2022).
- ²⁰A. Javadi and H. Nilsson, "LES and DES of strongly swirling turbulent flow through a suddenly expanding circular pipe," *Comput. Fluids* **107**, 301–313 (2015).
- ²¹P. S. Gnanbode, P. Orlandi, M. Ould-Rouiss, and X. Nicolas, "Large-eddy simulation of turbulent pipe flow of power-law fluids," *Int. J. Heat Fluid Flow* **54**, 196–210 (2015).
- ²²J. D. Sherwood, "Decay of turbulence in a power-law fluid," *Phys. Fluids* **28**, 753–754 (1985).
- ²³R. Chebbi, "Laminar flow of power-law fluids in the entrance region of a pipe," *Chem. Eng. Sci.* **57**(21), 4435–4443 (2002).
- ²⁴S. Yanuar, G. Mau, and M. Fachreza, "Rheological characteristics of non-Newtonian mud slurry flow using spiral pipes," *AIP Conf. Proc.* **2227**(1), 020001 (2020).
- ²⁵M. Sorgun, E. Ulker, S. O. K. Uysal, and T. D. Muftuoglu, "CFD modeling of turbulent flow for non-Newtonian fluids in rough pipes," *Ocean Eng.* **247**, 110777 (2022).
- ²⁶T. Dyakowski, G. Hornung, and R. A. Williams, "Simulation of non-Newtonian flow in a hydrocyclone," *Chem. Eng. Res. Des.* **72**(4), 513–520 (1994).
- ²⁷P. Filip and J. David, "Quasisimilarity of helical power-law fluid flow in concentric annuli," *AIP Conf. Proc.* **1152**(1), 86–95 (2009).
- ²⁸L. Yang, J. L. Tian, Z. Yang, Y. Li, C. H. Fu, Y. H. Zhu, and X. L. Pang, "Numerical analysis of non-Newtonian rheology effect on hydrocyclone flow field," *Petroleum* **1**(1), 68–74 (2015).
- ²⁹E. Taheran and K. Javaherdeh, "Experimental investigation on the effect of inlet swirl generator on heat transfer and pressure drop of non-Newtonian nanofluid," *Appl. Therm. Eng.* **147**, 551–561 (2019).
- ³⁰E. D. Hirleman, V. Oechsle, and N. A. Chigier, "Response characteristics of laser diffraction particle size analyzers: Optical sample volume extent and lens effects," *Opt. Eng.* **23**(5), 610–619 (1984).
- ³¹M. Wang, R. Mann, and F. Dickin, "Electrical resistance tomographic sensing systems for industrial applications," *Chem. Eng. Commun.* **175**, 49–70 (1999).
- ³²M. Brennan, "CFD simulations of hydrocyclones with an air core-comparison between large eddy simulations and a second moment closure," *Chem. Eng. Res. Des.* **84**, 495–505 (2006).
- ³³J. L. Yin, J. J. Li, Y. F. Ma, and D. Z. Wang, "Numerical approach on the performance prediction of a gas–liquid separator for TMSR," *J. Nucl. Sci. Technol.* **53**, 1134 (2015).
- ³⁴J. Zhang, Y. T. He, S. Liu, and J. Y. Xu, "Oil–water separation in a cylindrical cyclone with vortex finder," *Phys. Fluids* **34**(3), 033314 (2022).
- ³⁵S. Liu, J. Zhang, L. T. Hou, and J. Y. Xu, "Investigation on the variation regularity of the characteristic droplet diameters in the swirling flow field," *Chem. Eng. Sci.* **229**, 116153 (2021).
- ³⁶T. Wang, Z. Xia, and C. Chen, "Coupled CFD-PBM simulation of bubble size distribution in a 2D gas–solid bubbling fluidized bed with a bubble coalescence and breakup model," *Chem. Eng. Sci.* **202**, 208–221 (2019).
- ³⁷M. Dirzwager, "A new axial cyclone design for fluid–fluid separation," Ph.D. thesis (Delft University of Technology, Delft, 1996).